Magnetic Bulk Photovoltaic Effect in Bernal Bilayer Graphene

Yuncheng Mao^{1,*} and Claudio Attaccalite¹

¹CNRS/Aix-Marseille Université, Centre Interdisciplinaire de Nanoscience de Marseille UMR 7325 Campus de Luminy, 13288 Marseille Cedex 9, France (Dated: November 26, 2025)

Magnetic fields break time-reversal symmetry (TRS) and reshape a material's spatial symmetry. Because the bulk photovoltaic effect (BPVE) is exquisitely sensitive to symmetry, it offers a natural arena for magnetic-field control. Here, we explore how shift current (SC) and magnetic ballistic current (MBC) evolve and emerge in AB-stacked Bernal bilayer graphene subjected to in-plane and out-of-plane magnetic fields. We find that the SC responds only mildly to weak fields, behaving as an almost even function of field strength. In contrast, the MBC is activated directly by TRS breaking and grows linearly with weak fields at selected photon energies. Focusing on AB-bilayer graphene ribbon we investigate the behaviour of SC and MBC under both weak and strong vertical fields. We uncover the strikingly opposite roles played by edge states in the SC: under weak fields these highly localized, sublattice- and layer-polarized edge modes are essentially dark, yet under strong fields—when Landau levels dominate—the same edge states swell in spatial extent and become intensely bright contributors to the SC response.

I. INTRODUCTION

Conventional photovoltaic devices operate based on the pn-junction, where an internal electric field separates electron-hole pairs created by light absorption, driving a current through the circuit. The bulk photovoltaic effect (BPVE) offers a fundamentally different approach. As a second-order nonlinear optical response, BPVE generates a steady photocurrent directly in the bulk of a non-centrosymmetric material under uniform illumination. Rather than relying on a junction's field, the current in BPVE is driven by the intrinsic crystal symmetry that enables asymmetric electron excitation and relaxation. This unique property allows BPVE to produce photovoltages exceeding the band gap, offering a promising route to circumvent the Shockley-Queisser limit and achieve higher light-conversion efficiencies [1].

The absence of the centrosymmetry lies at the center of the mechanism of BPVE current [2–5]. This is one of the signs that BPVE is sensitive to the symmetrical properties of the physical system. Some examples of the non-centrosymmetric materials as good candidates are the transition metal dichalcogenides (TMD) [6–10] and the moiré materials [10–20]. The non-centrosymmetry can also be realized by changing the stacking manner of 2D materials without twist [21–23] or with heterojunctions of originally centrosymmetric materials [24]. Other materials with various compositions are also reported [25–33].

Two majors mechanisms contribute to the secondorder DC current, *i.e.* shift current (SC) and ballistic current [34]. The latter is often referred to as injection current (IC) in the presence of time-reversal symmetry (TRS) [35, 36], and has non-zero DC output only with circularly polarized light. Therefore, the shift current is usually the major dominant contribution to the DC current when the incident light is linearly polarized [4, 35, 37]. The application of the magnetic field to a physical system introduces many subtleties to the system. The external field may reduce the crystalline symmetry, and more importantly, breaks the TRS. BPVE under the magnetic field (therefore in the absence of TRS) is so far an under-investigated topic. Recent works show that the shift current is steady under the magnetic field, as long as the external field does not alter substantially the band structures [38, 39]. This scenario is referred to as the "weak-field regime" throughout this paper, as long as the modification to the band structure is minor and barely visible. The results of Dai et al. [39] show that the variation of the shift current has an interesting parabolic relation with the external field in the square-lattice model at certain photon frequencies. An important consequence of breaking the TRS with magnetic field is a newly enabled ballistic current that has a similar expression to the injection current (IC), hereafter named the magnetic ballistic current (MBC). IC and MBC are both linear in scattering time [35, 38-41]. In this paper we will stick to linearly polarized light and not discuss the injection current. We perform comprehensive analysis of SC and MBC under in-plane and vertical magnetic fields in the AB-stacked bilayer graphene, where the centrosymemtry is readily broken by the stacking.

The paper is organized as follows: In Section II, the AB-bilayer graphene model is explained with all the parameters specified. We then show the formulae and necessary ingredients for the computation of SC and MBC conductivity tensors. In Section III, we show the results and in-depth analyses of the current conductivity tensors and how they are influenced by the external field. This is followed by our statement of the main conclusions in Section IV.

^{*} catmyc@gmail.com

II. MODELS AND METHODS

In this section we explain the AB-stacked bilayer graphene model employed throughout this paper, as well as the formulae for computing SC and MBC conductivity tensors.

A. Model definition

To investigate how the in-plane magnetic field tunes the non-linear DC currents in the bilayer graphene, the following tight-binding model is employed:

$$\hat{H}_{AB-BG} = \sum_{\mathbf{R}\alpha l, \mathbf{R}'\alpha'l'} t_{\alpha'l'}^{\alpha l} (\mathbf{R} + \mathbf{d}_{\alpha l} - \mathbf{R}' - \mathbf{d}_{\alpha'l'}) c_{\mathbf{R}\alpha l}^{\dagger} c_{\mathbf{R}'\alpha l'},$$
(1)

where l and l' are the layer indices. $\alpha, \alpha' \in \{A, B\}$ denote the sublattice indices. \mathbf{R} and \mathbf{R}' are the Bravais lattice vectors of the honeycomb lattice, with

$$\mathbf{R}(n_1, n_2) = n_1 \mathbf{a}_1 + n_2 \mathbf{a}_2, \ n_1, n_2 \in \mathbb{Z},$$
 (2)

where $\mathbf{a}_{1/2} = [\pm 1/2, \sqrt{3}/2]^T \times 0.248$ nm, are the base vectors of the Bravais lattice of graphene single layer. $\mathbf{d}_{\alpha l}$ indicate the relative coordinate of sublattice α in layer l within each unit cell. Its values are enlisted here: $\mathbf{d}_{\mathrm{A,top}} = \mathbf{d}_{\mathrm{B,bottom}} = 0$, $\mathbf{d}_{\mathrm{B,top}} = 0.143\hat{\mathbf{y}}$ nm, and $\mathbf{d}_{\mathrm{A,bottom}} = -0.143\hat{\mathbf{y}}$ nm. The hopping term is given by

$$t_{\alpha'l'}^{\alpha l}(\mathbf{R} + \mathbf{d}_{\alpha l} - \mathbf{R}' - \mathbf{d}_{\alpha'l'}) = \sum_{j=1}^{3} \gamma_0' \delta_{ll'} \bar{\delta}_{\alpha \alpha'} \delta_{\mathbf{R} + \mathbf{d}_{\alpha l} - \mathbf{R}' - \mathbf{d}_{\alpha'l'}, \pm \mathbf{d}_j} + \text{interlayer terms}$$
(3)

where $\bar{\delta}_{\alpha\alpha'}=1-\delta_{\alpha\alpha'}$. The same convention is used for $\bar{\delta}_{ll'}$. We also define $\mathbf{d}_1=d[0,1]^T$, $\mathbf{d}_2=d[-\sqrt(3)/2,-1/2]^T$ and $\mathbf{d}_3=d[-\sqrt(3)/2,1/2]^T$, where d=0.143 nm is the C-C bond length in graphene single layer. The choice of \mathbf{d}_j vectors results in that the zig-zag edges of the graphene layer are aligned along the x-direction while the armchair edge is aligned along the y-direction. The interlayer hopping terms are enumerated below:

$$t_{\mathrm{A,bottom}}^{\mathrm{A,top}}(\boldsymbol{R}-\boldsymbol{R}'+\mathbf{d}_{1}) = \gamma_{4}' \sum_{j=1}^{3} \delta_{\boldsymbol{R}+\mathbf{a}_{j-1},\boldsymbol{R}'};$$

$$t_{\mathrm{B,bottom}}^{\mathrm{A,top}}(\boldsymbol{R}-\boldsymbol{R}') = \gamma_{1}' \delta_{\boldsymbol{R},\boldsymbol{R}'};$$

$$t_{\mathrm{A,bottom}}^{\mathrm{B,top}}(\boldsymbol{R}+\mathbf{d}_{1}-\boldsymbol{R}') = \gamma_{3}' \sum_{j=1}^{3} \delta_{\boldsymbol{R}+\mathbf{a}_{j},\boldsymbol{R}'};$$

$$t_{\mathrm{B,bottom}}^{\mathrm{B,top}}(\boldsymbol{R}+\mathbf{d}_{1}-\boldsymbol{R}') = \gamma_{4}' \sum_{j=1}^{3} \sum_{j=1}^{3} \delta_{\boldsymbol{R}+\mathbf{a}_{j-1},\boldsymbol{R}'},$$

where we have introduced $\mathbf{a}_0 = \mathbf{0}$ and $\mathbf{a}_3 = \mathbf{a}_1 + \mathbf{a}_2$. The hopping amplitudes are explicitly given with $\gamma_0' = -3.16$ eV, $\gamma_1' = -0.381$ eV, $\gamma_3' = -0.38$ eV and $\gamma_4' = 0.14$ eV. In Fig.1 we illustrate the bilayer graphene structure defined by these parameters.

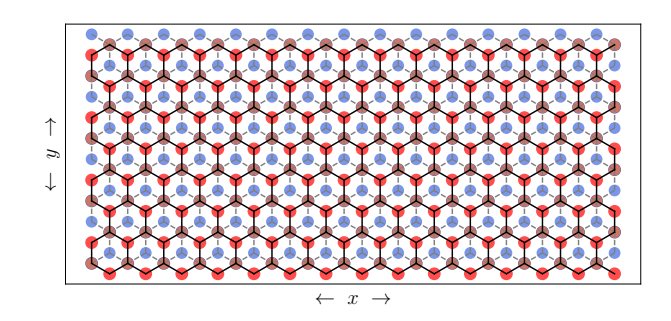


FIG. 1. Lattice structure of AB-stacked bilayer graphene. Solid lines show the connection between sublattices of the top layer, while gray dashed lines the bottom layer. The zigzag edges of graphene flakes are aligned along the x-direction, while the armchair edges are along the y direction. Orange dots mark the position of both A-sublattice of top layer and B-sublattice of bottom layer on the xy-plane. Red dots represent the B-sublattice of top layer. Light blue dots signifies the A-sublattice of the bottom layer.

To include the magnetic field, we employ the Peierls substitution on the hopping terms:

$$t_{\alpha'l'}^{\alpha l}(\mathbf{R} + \mathbf{d}_{\alpha l} - \mathbf{R}' - \mathbf{d}_{\alpha'l'})$$

$$\to t_{\alpha'l'}^{\alpha l}(\mathbf{R} + \mathbf{d}_{\alpha l} - \mathbf{R}' - \mathbf{d}_{\alpha'l'})e^{-i\frac{e}{\hbar}\int_{\mathbf{R}'+\mathbf{d}_{\alpha'l'}}^{\mathbf{R}+\mathbf{d}_{\alpha l}}\mathbf{A}\cdot\mathbf{d}\mathbf{r}}.$$
(4)

When uniform magnetic field is parallel to the graphene planes, the vector potential is given by

$$\mathbf{A}(z) = z\mathbf{B}_{\parallel} \times \hat{\mathbf{z}}.\tag{5}$$

With this convention, the vector potential is only a function of the z-coordinates, and is therefore constant within each layer. Performing the Fourier transform

$$c_{\mathbf{R}\alpha l} = \frac{1}{\sqrt{N}} \sum_{\mathbf{k}} e^{i\mathbf{k}\cdot(\mathbf{R} + \mathbf{d}_{\alpha l})} c_{\mathbf{k}\alpha l},$$

the Hamiltonian matrix is block diagonal in \boldsymbol{k} indices, with each diagonal block being

$$H_{AB}(\mathbf{k}) = \begin{bmatrix} \Delta + \frac{\Delta'}{2} & \gamma'_0 g(-\mathbf{k} + \mathbf{k}_0) & \gamma'_4 g(\mathbf{k}) & \gamma'_1 \\ \gamma'_0 g(\mathbf{k} - \mathbf{k}_0) & \Delta - \frac{\Delta'}{2} & \gamma'_3 g(-\mathbf{k}) & \gamma'_4 g(\mathbf{k}) \\ \gamma'_4 g(-\mathbf{k}) & \gamma'_3 g(\mathbf{k}) & -\Delta - \frac{\Delta'}{2} & \gamma'_0 g(-\mathbf{k} + \mathbf{k}_0) \\ \gamma'_1 & \gamma'_4 g(-\mathbf{k}) & \gamma'_0 g(\mathbf{k} - \mathbf{k}_0) & -\Delta + \frac{\Delta'}{2} \end{bmatrix},$$
(6)

where

$$\mathbf{k}_0 = \frac{e}{\hbar} \mathbf{A} \left(\frac{L_z}{2} \right) \tag{7}$$

is the effective momentum shift on the top layer. $L_z=0.335$ nm is the vertical distance between the two graphene sheets. In Eq. (6), we have chosen z=0 to be exactly in the middle between the two layers. With

this choice, the interlayer hopping terms acquire zero net phase upon the Peierls substitution. Throughout this work we add a layer offset potential $\Delta=0.4$ eV to simulate the vertical static electric field. A sublattice offset potential $\Delta'=0.022$ eV is also applied to simulate the effects of the hBN substrate sandwiching the BG system.

In the case of the perpendicular magnetic field $\boldsymbol{B}=B\hat{\boldsymbol{z}}$, we use a AB-BG ribbon to investigate the current response to avoid the difficulty of huge magnetic unit cells. We have chosen to impose a cut off along the y-direction. Therefore, the nanoribbon has zig-zag edges on both sides, which is known to host edge states. We later show with explicit calculations that the edges states will not contribute to current response. The Landau gauge is used to describe the perpendicular magnetic field, i.e.

$$\boldsymbol{A} = y\boldsymbol{B}_{\perp} \times \hat{\boldsymbol{y}} = -yB\hat{\boldsymbol{x}} \tag{8}$$

The vector potential in this case is a function of y coordinates but aligned along the x-direction.

B. Shift current, injection current and magnetic ballistic current

Three types of DC current may exist. The shift current (SC) and the injection current (IC) are the two discussed the most frequently. Upon the application of the magnetic field that breaks the time reversal symmetry, a third current, named "magnetic ballistic current" (MBC) in literature [39], is also enabled [38, 39]. The detailed derivation of the shift current and injection current conductivity tensors in a system with time-reversal symmetry has been well established in the past decades in different formalisms [35, 36, 42]. The shift current conductivity is given by

$$\sigma^{abc}(\omega) = -\frac{i\pi e^3}{\hbar^2} \int \frac{\mathrm{d}^D \mathbf{k}}{(2\pi)^D} \times \sum_{nm} f_{nm} \left[r_{mn}^b r_{nm;a}^c + r_{mn}^c r_{nm;a}^b \right] \delta(\omega_{mn} - \omega), \tag{9}$$

where $a,b,c\in\{x,y,z\}$. The **k**-dependence of the physical quantities inside the integrand is not shown explicitly for simplicity. D denotes the dimension of the system. $r_{mn}^b = i \langle u_m | \partial_b | u_n \rangle$ is called the interband Berry connection, where ∂_b is a short-hand notation for ∂_{k_b} . $r_{nm;a}^b$ is the generalized derivative of r_{nm}^b defined by $r_{nm;a}^b = -i[A_{nn}^a - A_{mm}^a - \partial_a]r_{nm}^b$, where we have introduced the usual intraband Berry connection $A_{nn}^a = i \langle u_n | \partial_a | u_n \rangle$. $r_{nm;a}^b$ can be further computed with $r_{nm;a}^b = [\partial_a - i(A_{nn}^a - A_{nm}^a)] r_{nm}^b = -iR_{nm}^{a;b} \times r_{nm}^b$, where the shift vector $R_{nm}^{a;b}$ appears explicitly:

$$R_{nm}^{a;b} = A_{nn}^a - A_{mm}^a - \partial_a \operatorname{Arg} \left[r_{nm}^b \right]. \tag{10}$$

It indicates a displacement, *i.e.* a "shift", in the real space due to the transition between bands n and m.

 $f_{nm} = f_n - f_m$, with f_n being the Fermi-Dirac distribution function of energy level $E_{n\mathbf{k}}$. ω_{mn} is simply $(E_{m\mathbf{k}} - E_{n\mathbf{k}})/\hbar$.

The IC conductivity tensor can be computed with

$$\eta^{abc}(\omega) = \frac{2\pi e^3}{\hbar^2} \sum_{nm} \int \frac{\mathrm{d}^D \mathbf{k}}{(2\pi)^D} \times \mathcal{V}_{mn}^a f_{nm} \operatorname{Im} \left[r_{mn}^c r_{nm}^b \right] \delta(\omega_{mn} - \omega), \tag{11}$$

where $\mathcal{V}^a_{mn} = v^a_{mm} - v^a_{nn}$, with the velocity matrix being $v^a_{mn} = \langle u_m | \partial_a H | u_n \rangle / \hbar$. This also enables the evaluation of the interband connection with $r^a_{mn} = -iv^a_{mn}/\omega_{mn}$, $m \neq n$. We remark that IC tensor is antisymmetric to the permutation of indices b and c, i.e. $\eta^{abc} = -\eta^{acb}$. IC tensors of type η^{abb} are always zero. The direct consequence of this property is that injection current in a system must be created by shedding circularly polarized light into the system.

The MBC is a previously under-discussed quantity as it is often forbidden by the time-reversal symmetry (TRS). The magnetic field breaks TRS and allows non-zero MBC response in the physical system. The MBC tensor is similar to the IC tensor, and writes

$$\zeta^{abc} = \frac{2\pi e^3}{\hbar^2} \sum_{nm} \int \frac{\mathrm{d}^D \mathbf{k}}{(2\pi)^D} \times$$

$$\mathcal{V}_{mn}^a f_{nm} \operatorname{Re} \left[r_{mn}^c r_{nm}^b \right] \delta(\omega_{mn} - \omega) .$$
(12)

In above expressions of the three conductivity tensors, we consider D=2 for the 2D periodic system.

To compute the current response tensor in nanoribbons, it suffices to replace $\mathrm{d}^2 \boldsymbol{k}/(2\pi)^2$ with $\mathrm{d} k/(2\pi L)$ in these expressions, where L is the width of the nanoribbons. The integral is then performed in the 1D Brillouin zone for the nanoribbons. In this way the conductivity tensors have the same dimension whether we treat a 2D periodic system or a nanoribbon retaining periodicity along only one direction.

In this paper we will focus on the scenarios where the light is linearly polarized. Therefore, the injection current is *always* zero. But we remark that the same methodology is can be easily applied to the analyses of the influence of magnetic field on the injection current under circularly polarized light.

III. RESULTS AND DISCUSSION

A. Symmetry constraints on current response

Let us first understand why in-plane magnetic field can be interesting for bilayer graphene. When the magnetic field in parallel with the graphene planes, the magnetic flux is zero within every hexagonal plaquette. The magnetic field induces a non-zero phase along each C-C bond, but the total phase accumulated in a plaquette always

cancels out. Therefore there is no magnetic supercell. If we look at the single layer graphene, the phases created by the magnetic field can be conveniently gauged out by a global shift of the coordinates in the momentum space, therefore the in-plane magnetic field has no effect on single layer graphene. But with two graphene layers stacked together, the situation becomes much more interesting: the momentum shift in each layer is different, and therefore can not be gauged out by one-single global shift in the whole system.

In Fig. 2 we show that under the application of a magnetic field the electronic band structure remains essentially unchanged unless the field strength is pushed to unrealistically large values (on the order of 10³ T). Despite this negligible influence on the band dispersions themselves, the magnetic field nevertheless breaks certain symmetries of the system. This symmetry reduction can have nontrivial consequences for the nonlinear current response, which is the central focus of our investigation.

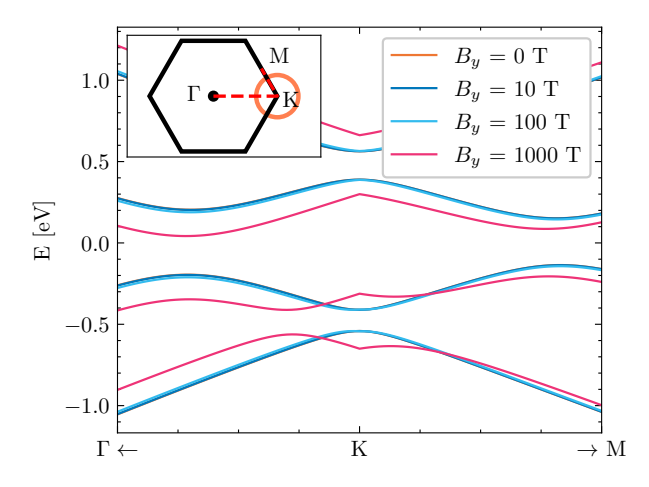


FIG. 2. Band structure of AB-BG under different magnetic field along y direction with intensity ranging from 0 to 1000 Tesla. The band structures are not shown for the whole route $\Gamma - K - M$. Only the part inside in the orange circle is presented to concentrate on the band structures near the Fermi level (as we have set the chemical potential $\mu = 0$). No substantial change can be found on the band structures unless the magnetic field is unrealistically strong.

Before applying the magnetic field and computing the current tensors, it is essential to analyze the symmetry of the system and identify the independent components of each current tensor. We first remark that the AB-BG model employed here breaks the spatial inversion symmetry, thus enabling non-zero second-order current responses. In the absence of the magnetic field, the AB-BG preserves C_3 rotational symmetry. To identify the independent components of the *in-plane* current tensors, it suffices to apply the following relation to all conductivity tensor components:

$$\iota^{abc} = R_{aa'}^{-1} \iota^{a'b'c'} R_{b'b} R_{c'c} \tag{13}$$

and impose $\iota^{abc} = \iota^{a'b'c'}$, where $\iota = \sigma, \eta$ or ζ , and

 $a,b,c,a',b',c' \in \{x,y\}$. R is the orthogonal matrix rotating a vector by $2\pi/3$ in the xy-plane, given by

$$R = \begin{bmatrix} -1/2 & -\sqrt{3}/2 \\ \sqrt{3}/2 & -1/2 \end{bmatrix}.$$

In this way we identify two groups of independent fully in-plane components:

$$\iota^{xxx} = -\iota^{yxy} = -\iota^{yyx} = -\iota^{xyy},\tag{14}$$

$$\iota^{yyy} = -\iota^{xxy} = -\iota^{xyx} = -\iota^{yxx}. (15)$$

Given the injection conductivity tensors are antisymmetric to the exchange of the indices of the electric field, η^{abc} is zero if a, b and $c \in \{x, y\}$. The application of the inplane magnetic field breaks the C_3 rotational symmetry, and perturbs the equality shown in Eqs. (14) and (15).

B. Current response with in-plane magnetic field

We first investigate how the shift current is influenced by the in-plane magnetic field. In the absence of magnetic field, the most remarkable shift current response is σ^{yxx} . We focus on its variation under different strengths of the magnetic field. We first align the magnetic field along the y-direction and vary its strength from -10 to 10 Tesla. We show the evolution of σ^{yxx} under different strengths of the magnetic field in Fig. 3. The shift current response appears to be an even function of the magnetic field. This is very similar to the calculations of Dai et al [39]. But here we cannot confirm a parabolic relation between the shift current and the magnetic field intensity. The trend of shift current as a function of the magnetic field is more complicated and differs at different photon energies. In Fig. 3(b) and (c), we track the variation of the largest peak located at $\omega = 0.32$ eV and 0.42 eV, respectively. The variation of $\sigma^{yxx}(\omega = 0.32 \text{ eV})$ does not show parabolic trends with the magnetic field. While the $\Delta \sigma^{yxx}(\omega = 0.42 \text{ eV})$ is an approximate even function of B, but it shows almost linear trend on both sides of B=0.

In Fig. 4, we explore how the external magnetic field affects the joint density of states (JDOS). The joint density of states is calculated with

$$\mathcal{J}(\omega) = \int \frac{\mathrm{d}^2 \mathbf{k}}{(2\pi)^2} \sum_{nm} f_{nm} \delta(\omega - \omega_{mn}). \tag{16}$$

Varying the magnetic field from -10 to 10 Tesla, the modification of the landscape of JDOS is also minor. As suggested by Fig. 4(b), the modification to the JDOS is $3 \sim 4$ orders of magnitude smaller than the JDOS at zero magnetic field. We note that the variation of JDOS is also an *even* function of the magnetic field, similar to the change of shift current brought by the magnetic field.

We then investigate the impact of the magnetic field on the shift vector. To focus on the interband transitions responsible to the shift current within the light frequency range between 0 and 2 eV. We focus on the shift

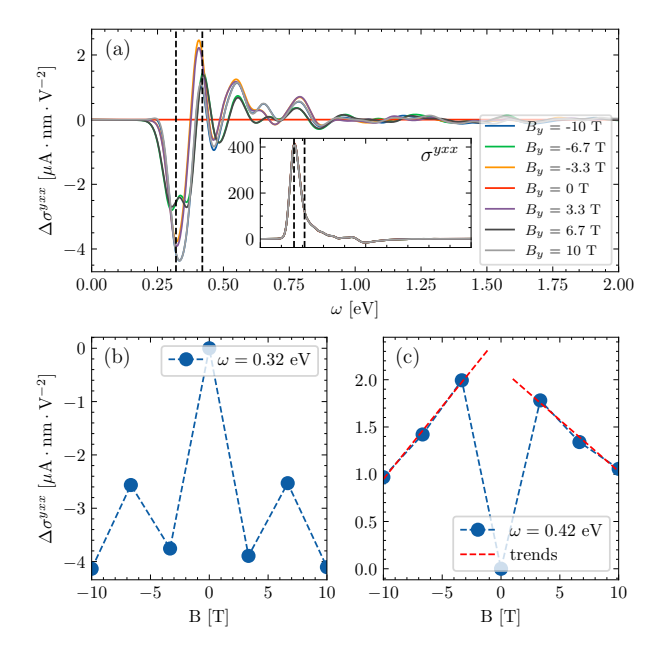


FIG. 3. (a) The variation of σ^{yxx} with respect to zero magnetic field. In the inset plot of (a) we also show the complete curve of σ^{yxx} under different magnetic field. The vertical dashed lines indicate the photon energies at which we track the variation of σ^{yxx} in (b) and (c), respectively. (b) The variation of σ^{yxx} with photon energy fixed at $\omega=0.32$ eV. (c) The variation of σ^{yxx} with photon energy fixed at $\omega=0.42$ eV.

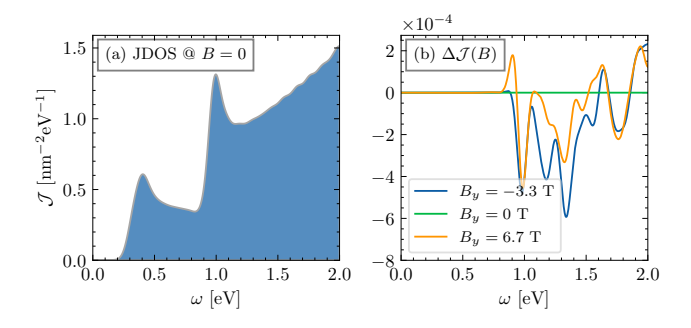


FIG. 4. (a) JDOS of AB-BG in the absence of external magnetic field. (b) The variation of JDOS under different intensity of the magnetic field with respect to the zero-field JDOS.

vector connecting the two middle bands (the highest occupied and the lowest unoccupied bands), noted R_{23}^{yx} . In Fig. 5(a) we show the distribution of R_{23}^{yx} in the vicinity of the K point of AB-BG. We focus on this region because only the parts of the bands near K and K' points contribute to the photovoltaic response within the photon energy range of interest. The variation of the shift vector upon the application of the magnetic field of 10 Tesla along the y direction is shown in Fig. 5(b).

The results above suggest that the shift current is stable and is only slightly altered by the magnetic field, as long as the latter is not strong enough to significantly alter the band structure. In the following we show a

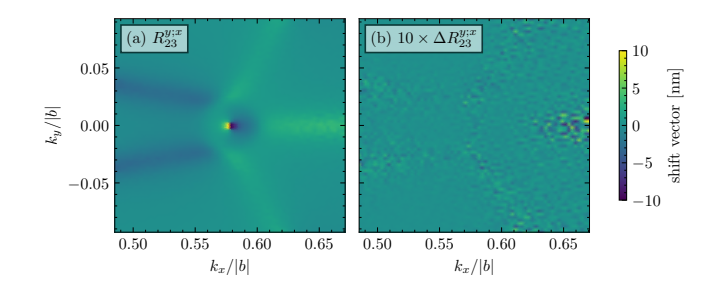


FIG. 5. (a) Shift vector R_{23}^{yx} distribution near K point of ABBG in the absence of magnetic field. (b) The variation of the shift vector. Data are exaggerated by a factor of 10 for better visibility. Here $|b|=4\pi/3d$ is the length of the reciprocal lattice base vector of AB-BG, with d=1.43 Å being the C-C bond length in the graphene sheet.

newly enabled second-order DC current response due to the breaking of time-reversal symmetry (TRS), referred to as magnetic ballistic current (MBC).

In Fig. 6(a), we show the MBC conductivity ζ^{xyy} under different magnetic field strengths. The MBC response is strictly zero when B=0, as it is forbidden by TRS. Tracing the evolution of the MBC conductivity as a function of the magnetic field, MBC is shown to scale linearly to the intensity of this external field, as is indicated by Fig. 6(b) and (c).

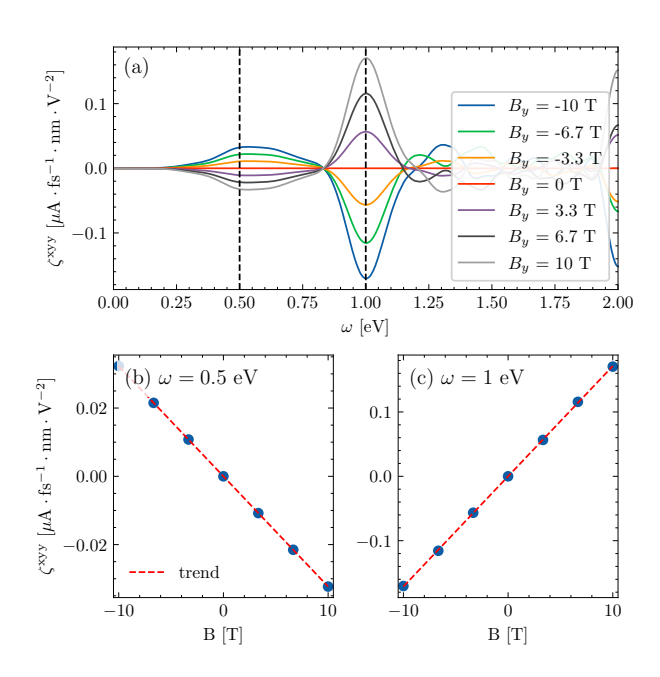


FIG. 6. (a) MBC response ζ^{xyy} enabled by the external inplane magnetic field. (b) and (c) show respectively ζ^{xyy} fixed at $\omega = 0.5$ and 1 eV. A well pronounced linear relation with the magnetic field is found at both frequencies.

C. Current in AB-BG nanoribbons with vertical magnetic field

The direct computation of the band structure of AB-BG in the perpendicular magnetic field is hindered by the problem of the extremely large magnetic unit cell. Therefore we turn to the AB-BG nanoribbon to investigate how the photovoltaic current is influenced by the perpendicular external field. To do so, boundaries along the y-direction are imposed on Eq. (1), i.e. we limit the y coordinates to be $0 \le y \le L_y$, with L_y being the width of the nanoribbon. We ensure that in both graphene sheets, the zig-zag edges are on the boundaries. The Hamiltonian is now periodic along the x-direction, and the band structure can be computed as a function of k_x . We recall that the same layer offset of 0.4 eV and sublattice offset of 0.022 eV is also applied to keep consistency throughout this work.

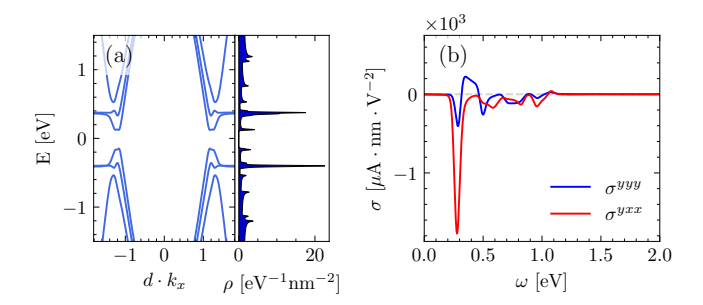


FIG. 7. (a) The band structure and the associated density of states of an AB-stacked bilayer graphene nanoribbon with its width being 41.89 Å. The localized edge modes manifest themselves as the flattened parts of the middle bands. (b) The shift current components σ^{yyy} (blue) and σ^{yxx} (red) computed in AB-BG nanoribbon.

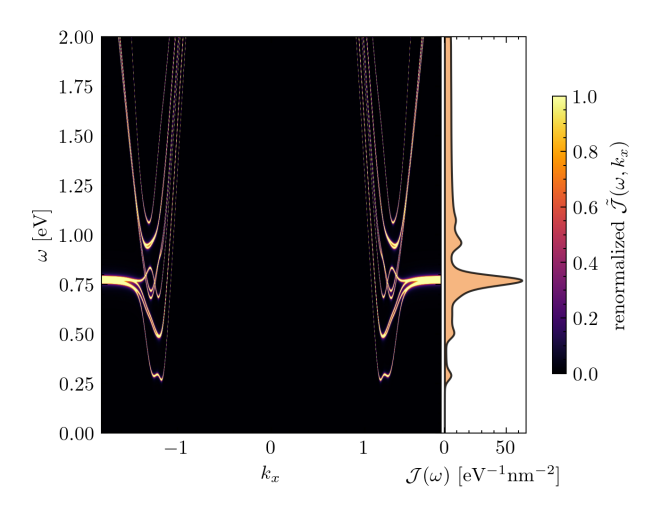


FIG. 8. Color plot of the detailed joint density of states of AB-BG nanoribbon, accompanied by the JDOS obtained by integrating the former over the Brillouin zone The values of the detailed JDOS are renormalized to the interval [0, 1] for simplicity of presentation.

In Fig. 7(a) we show the band structure and the density of states of a AB-BG nanoribbon, where the width of the ribbon has been set to 41.89 Å. The shift current conductivity tensors σ^{yyy} and σ^{yxx} are presented in Fig 7(b). Due to the cut in the y-direction, the C_3 symmetry is brutally broken. σ^{yyy} and $-\sigma^{yxx}$ are no longer equal. The mirror symmetry \hat{M}_y sending $x \to -x$ forbids the shift current along the x-direction in the absence of the magnetic field.

An interesting observation is that the remarkable density of states and joint density of states (JDOS) contributed by the edge states are not manifested in the shift current response. The JDOS profiles are shown in Fig. 8, where we show also a color plot of the energy-resolved joint density of states extracted from Eq. (16), defined as

$$\tilde{\mathcal{J}}(\omega, k_x; \Gamma) = \frac{1}{\pi} \sum_{nm} \frac{\Gamma f_{nm}}{(\omega - \omega_{mn})^2 + \Gamma^2}, \quad (17)$$

where the broadening factor Γ has been chosen to be 2 meV to generate the color plot. JDOS is then obtained by integrating $\tilde{\mathcal{J}}(\omega, k_x)$ over the Brillouin zone and taking the limit $\Gamma \to 0^+$:

$$\mathcal{J}(\omega) = \lim_{\Gamma \to 0^+} \int \frac{\mathrm{d}k_x}{2\pi L_y} \tilde{\mathcal{J}}(\omega, k_x; \Gamma).$$

Although the remarkable DOS and JDOS (Fig. 8) from edge states is potentially in favor of a strong SC response at around 0.75 eV, no shark peak is found in the SC spectra near this light frequency. This is because the edge states are highly polarized in both layer and sublattices, thus rendering the matrix elements of the position operator $r_{nm} = i \langle u_n | \hat{r} | u_m \rangle = 0, \ \forall n \neq m$ for edge states. The edge states are thus "dark" in the SC response.

In Fig. 9 we show the shift current conductivity component σ^{yxx} under different vertical magnetic field strengths ranging from -10 to 10 Tesla along the zdirection. We trace the variation of σ^{yxx} at two fixed photon frequencies, $\omega = 0.48 \text{ eV}$ and $\omega = 0.95 \text{ eV}$ in Figs. 9 (b) and (c) respectively. We observe again the variation of the shift current conductivity as an even function of the magnetic field. But the relation between $\Delta \sigma^{yyy}$ and B_z differs by light frequency. At $\omega = 0.48$ eV, a roughly linear relation is found on both sides of the $B_z = 0$. In contrast, a well-fit parabolic relation is manifested if the light frequency is fixed at $\omega = 0.95$ eV. Examining other light frequencies may show more complicated relations (not shown in the main text), but the even-function feature is retained. We have experimented both fittings with linear and parabolic trends. The trend shown in Fig. 9 is determined by the one greater R^2 value.

Following the same spririt of the energy resolved JDOS, we perform an energy-momentum resolution analysis of the shift current component σ^{yxx} in Fig. 16(a), where we comput and show the momentum-resolved SC

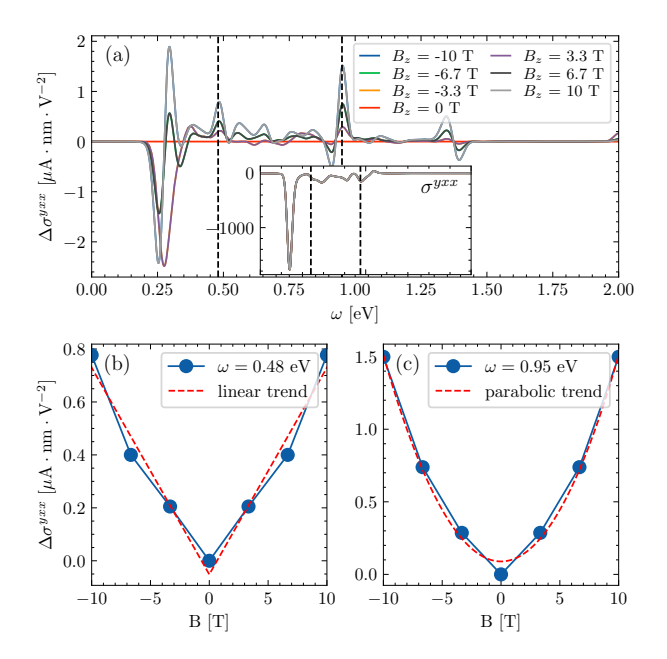


FIG. 9. (a) The main plot shows the variation of σ^{yxx} with respect to zero magnetic field in the AB-stacked zigzag nanoribbon. In the inset plot we also show the complete plots of σ^{yxx} under different magnetic field. The vertical dashed lines indicate the photon energies at which we track the variation of σ^{yxx} in (b) and (c), respectively. (b) The variation of σ^{yxx} with photon energy fixed at $\omega=0.48$ eV. An approximate linear relation is found between $\Delta\sigma^{yxx}(\omega=0.48$ eV) on both sides of $B_z=0$. (c) The variation of σ^{yxx} with photon energy fixed at $\omega=0.95$ eV. A parabolic relation between $\Delta\sigma^{yxx}(\omega=0.95$ eV) and the magnetic field is reported, similar to the observations in Ref. [39].

tensor $\tilde{\sigma}^{yxx}(\omega, k_x)$ given by:

$$\tilde{\sigma}^{yxx}(\omega, k_x) = \frac{1}{\pi} \sum_{nm} \frac{R_{nm}^{yx} |r_{nm}^x|^2 \Gamma}{(\omega - \omega_{mn})^2 + \Gamma^2}.$$
 (18)

Here we have adopted a broadening factor of $\Gamma=5$ meV. Comparing the photon energy of the hot spots in Fig. 10(a) (at ~ 0.25 eV) with the band structure, it is straightforward to see that the intense shift current response can only originate from the transition between the top of the highest valence band and the bottom of the lowest conduction band. In Fig. 10(b), we further investigate the shift vector $R_{\rm lc,\ hv}^{yx}$ and the interband connection $r_{\rm lc,\ hv}^x$ contributed by the two middle bands, where "lc" and "hv" stand for the "lowest conduction band" and "highest valence band", respectively.

Fig. 10(b) also explained why the localized edge states do not contribute to the shift current in spite of their high density of states. This is because the edge states (at both ends of the Brillouin zone) contribute the zero shift vector and almost zero interband connection. Approaching the bottom/top of the conduction/valence band, both the shift vector and the interband connection start to acquire non-zero values. At exactly the bottom/top of the conduction/valence band, both R^{yx} and r^x have significant

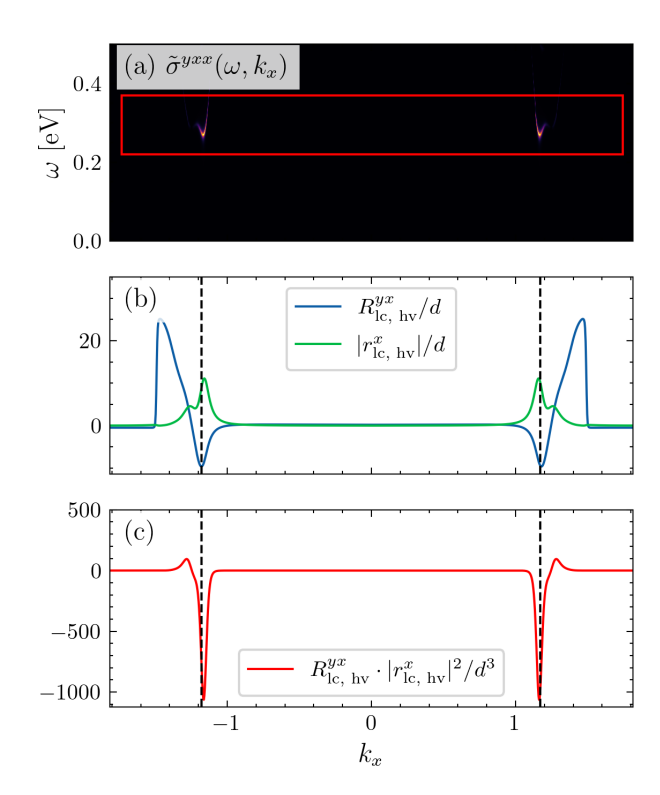


FIG. 10. (a) Color plot of $\tilde{\sigma}^{yxx}(\omega, k_x)$. (b) Shift vector (blue) and the absolute values of the interband connection (green) computed for the two middle bands. (c)Product of the shift vector and module square of the interband connection between the middle bands. The vertical dashed lines in (b) and (c) indicate the location of the bottoms of lowest conduction band, which are also the tops of the highest valence band.

magnitude. This gives rise to an intense SC response near 0.25 eV.

In Fig. 11 we show the analysis of MBC response of the AB-BG nanoribbon to the vertical magnetic field. The MBC conductivity tensor ζ^{xyy} under different field intensity is plotted in Fig. 11(a). In Fig. 11(b) and (c) we track the value of ζ^{xyy} at fixed light frequencies 0.52 and 0.95 eV, respectively. Linear relation between MBC and the vertical field is also found.

D. Current under strong magnetic field with Landau levels

To make the Landau levels manifest themselves in the bilayer graphene layers without any relative twist between the layers, the magnitude of the magnetic field need to be unrealistically high so as to create a significant magnetic flux per unit cell. Although this is experimentally difficult to achieve, we can investigate the Landau-level effects on SC and MBC in a theoretical manner.

We apply a vertical magnetic field of 1000 T to the AB-BG nanoribbon, and show the resulted band structure with density of states as well as the shift current in Fig. 12. The magnetic ballistic current response tensors

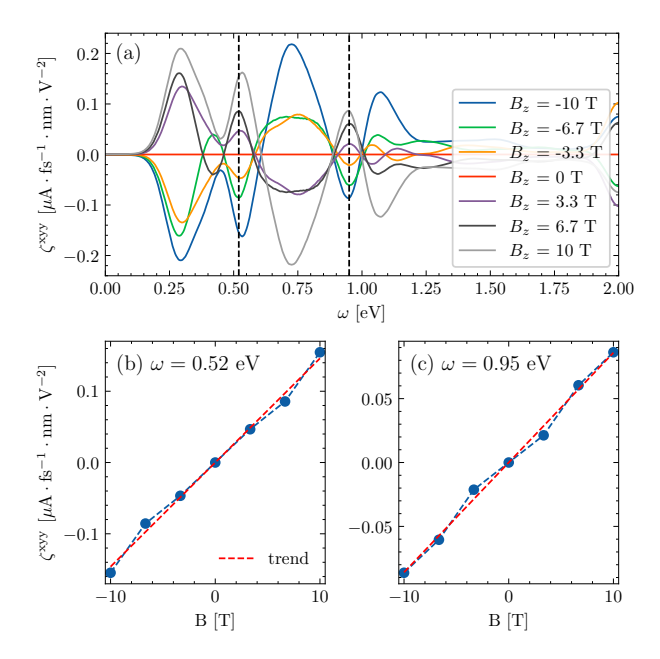


FIG. 11. (a) MBC response ζ^{xyy} enabled by the external in-plane magnetic field in the AB-stacked zigzag ribbon. (b) and (c) show respectively ζ^{xyy} fixed at $\omega=0.52$ and 0.95 eV. Linear relation between the MBC current and the vertical magnetic field is also found.

are reported in Fig. 13. The magnetic flux per plaquette is $\Phi/\Phi_0 = 0.0128$, where $\Phi_0 = h/e \approx 4.135 \times 10^{-15}$ Wb is the flux quantum. In order to stress on the flattened bands by the Landau levels, the width of the nanoribbon is increased to 63.19 Å.

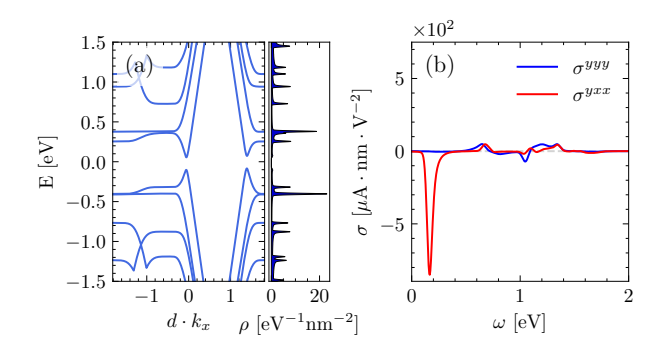


FIG. 12. (a) The band structure and the associated density of states of an AB-BG nanoribbon placed in strong vertical magnetic field of 1000 T. Band flattening by Landau levels under strong magnetic field is very remarkable, leading to very spiky DOS profile. (b) The shift current components σ^{yyy} (blue) and σ^{yxx} (red) computed in AB-BG nanoribbon.

In Fig. 14, we also show the energy-resolved JDOS and the JDOS of the AB-BG in strong vertical magnetic field. In both profiles of the DOS in Fig. 12(a) and the JDOS in Fig. 14, the enhanced density of states brought by the Landau-level flattened bands are substantial.

However, similar to our previous observation of the

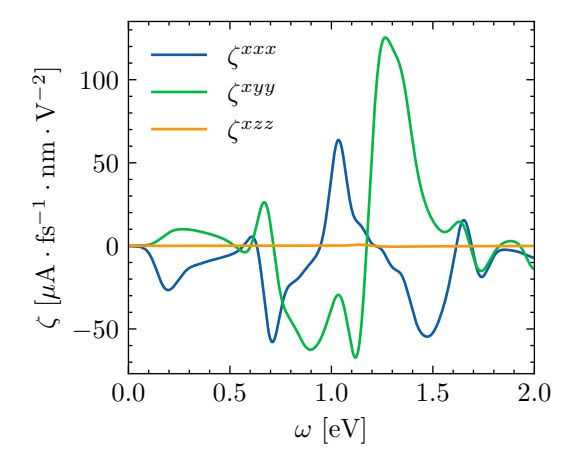


FIG. 13. MBC in AB-BG nanoribbon under strong magnetic field. The magnitude of MBC is large due to the extremely strong field. The ζ^{xyy} curve has no resemblance to those in Fig. 11, implying that the linear relation is broken as substantial band reconstruction happens.

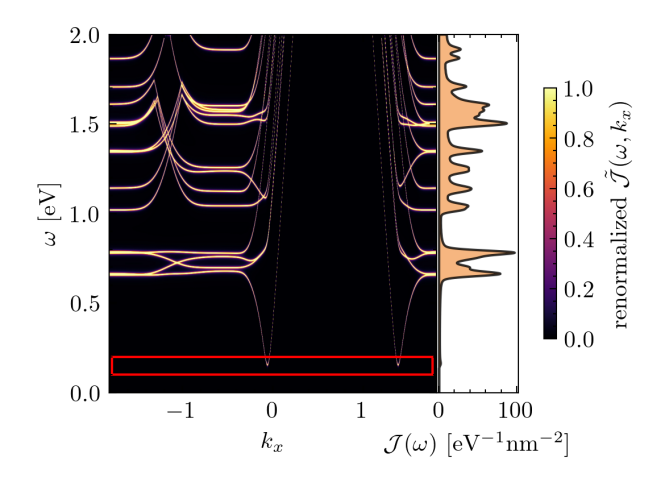


FIG. 14. Heatmap of the detailed joint density of states of AB-BG nanoribbon placed in vertical magnetic field of 1000 T. Heatmap is accompanied by the JDOS obtained by integrating the former over the Brillouin zone. The values of the detailed JDOS are renormalized to the interval [0,1] for simplicity of presentation. The red rectangle highlights the photon energy range where the largest peak of σ^{yxx} appears (~ 0.15 eV).

edge-state contribution to the shift current, the localized Landau levels are *not* able to boost the SC response as the JDOS profile suggests. The strongest SC peak of σ^{yxx} appears at around 0.155 eV. Near this photon energy, the JDOS is in fact sparse, as highlighted by the red rectangle in Fig. 14. After examining the band structure in Fig. 12(a), it turns out that only the transition between two pairs of states located at band edges, i.e. the bottom of the lowest conduction band and the top of the highest valence band, contributes to this intense peak.

In Fig. 15, we show the wave function distribution along the y-direction for the states contributing to the

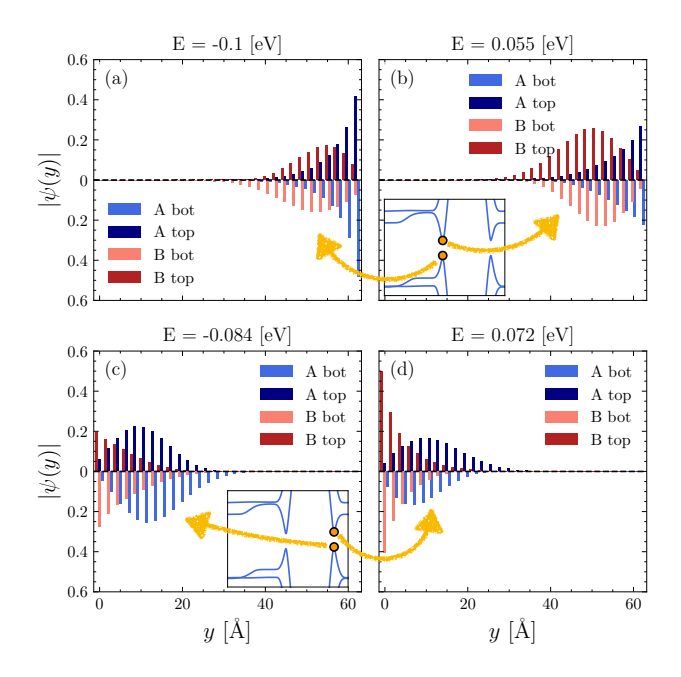


FIG. 15. The wave functions amplitudes of the two pairs of states contributing to the largest peak of σ^{yxx} . (a) and (c) correspond to the two states located at the top of the valence band, while (b) and (d) are the states at the bottom of the conduction band. Their locations in the band structure are also indicated with yellow dots. The arrows show explicitly the yellow points and the wave functions. In each subfigure, the upper half show the amplitudes of the wave function on the top layer while those of the bottom layer are presented on the lower half. Wave functions living on sublattices A and B are colored blue and red, respectively.

largest peak of σ^{yxx} . It is then intuitive to understand that the overlap of within each pair of wave functions leads to considerable matrix element values of $y_{mn} = \langle u_m | y | u_n \rangle$, despite the relatively weak JDOS.

The hot spots appear exactly at the photon energy ~ 0.16 eV, corresponding to the separation between the band edges of lowest conduction band and the highest valence band. Therefore we examine the shift vector R^{yx} and the interband connection r^x between the two middle bands, and the results are shown in Fig. 16(b). It is then clear that the interband connection and the shift vector can be simultaneously non-zero near the narrowest band gaps, resulting in only two sharp peaks shown in Fig. 16(c). This leads to the sharp intense peak in σ^{yxx} observed in Fig. 12(b). An important remark is that the sharp peak of σ^{yxx} comes from the edge states, which is exactly the opposite to the weak-field scenario.

The fact that the sharp peak originates fully from the transition between the edge states belong to different bands can be verified by the dilution effect. The number of the edge states is fixed, and therefore the DOS and JDOS from them will be diluted as the width of the nanoribbon grows. Therefore, we expect the intense peak to be *inversely* proportional to the width. In Fig. 17, we compute and show σ^{yxx} for different widths of the

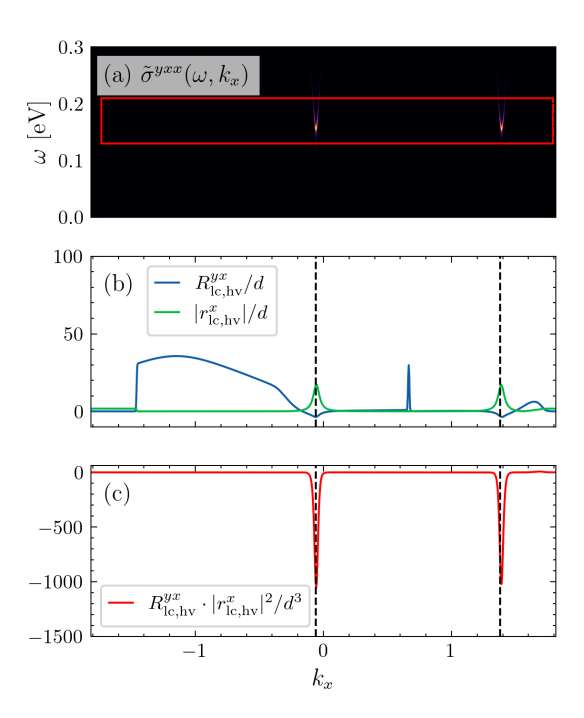


FIG. 16. (a) Color plot of $\tilde{\sigma}^{yxx}(\omega, k_x)$. (b) Shift vector (blue) and the absolute values of the interband connection (green) computed for the two middle bands. (c) Product of the shift vector and module square of the interband connection between the middle bands. The vertical dashed lines in (b) and (c) indicate the location of the bottoms of lowest conduction band, which is also the tops of the highest valence band.

nanoribbon. In the inset we show the peak intensity as a function of the $1/L_y$ with L_y denoting the width of the ribbon. A perfect linear relation is found between the peak intensity and the inverse of the ribbon width, proving that the sharp intense peak is due to the transition between edge states.

It is then interesting to notice that under no or weak vertical magnetic field, the edge states are extremely localized and do not contribute to the shift current response. The other states in the electronic band are diffusive and can generate significant SC response. In great contrast, in the presence of strong magnetic, the scenario become reversed. The edge states acquire now substantial spatial extent, allow them to have non-zero overlap in space, and eventually intense peaks in the SC response. In both weak- and strong-field scenarios, the strong SC responses come always from the band edges, despite their different origins. This is coherent with the designing principles of giant SC response proposed by Cook et al [43].

IV. CONCLUSION

We have investigated the shift current and magnetic ballistic current in AB-BG bulk and nanoribbon, in the absence and the presence of the external magnetic field.

In the weak-field regime, we identify an even-function

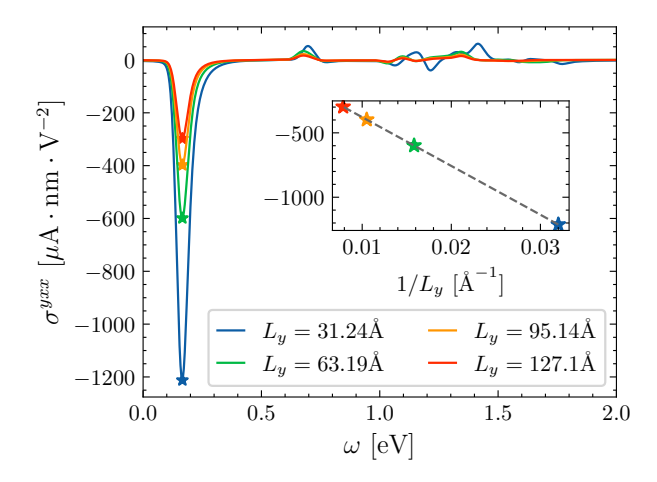


FIG. 17. σ^{yxx} with different ribbon widths. Vertical magnetic field is fixed at 1000 T. The inset show the plot of the peak intensity as a function of the inverse of the ribbon width, demonstrating perfect linearity. The inset plot validates the dilution effect by increasing the ribbon width, and therefore supports our argument that the intense peak originates solely from the edge states.

feature of the variation of the shift current as a function of the external field. A linear function or parabolic function can be found according to the photon energy chosen. But no universal law is found here. The breaking of the timereversal symmetry enables a magnetic ballistic current. We found linear relation between MBC and the external field. But note that the validity of the linearity also depends on the photon energy chosen. In the presence of vertical magnetic fields, we have investigated both weak and strong fields and made comprehensive comparison. It is found that the edge states play exactly the opposite roles in both scenarios. They are "dark" in weak field due to their localization and polarization on the sublattices and layers. On the contrary, strong magnetic field localized the other states to Landau levels but endows edges states with substantial spatial distribution, giving rise to an intense SC response. The contribution to the SC response from edge states is confirmed by the dilution effect with increasing ribbon width. An important message taken is that high JDOS can be deceptive. Only high JDOS from diffusive states can contribute significantly to the SC response. JDOS from localized states either from edge states or from Landau levels - has negligible contribution to SC as their interband connection is extremely small.

We expect that our findings will be relevant not only for AB-BG in a magnetic field, but also for graphene van der Waals heterostructures, where a magnetic field can be generated by the proximity effect (see, for example, Ref. [44]).

ACKNOWLEDGMENTS

C.A. and Y.M. acknowledge ANR project COLIBRI No. ANR-22-CE30-0027. C.A. acknowledges funding from European Research Council MSCA-ITN TIMES under grant agreement 101118915.

- A. Pusch, U. Römer, D. Culcer, and N. J. Ekins-Daukes, Energy conversion efficiency of the bulk photovoltaic effect. PRX Energy 2, 013006 (2023).
- [2] W. Kraut and R. von Baltz, Anomalous bulk photovoltaic effect in ferroelectrics: A quadratic response theory, Phys. Rev. B 19, 1548 (1979).
- [3] V. I. Belinicher and B. I. Sturman, The photogalvanic effect in media lacking a center of symmetry, Soviet Physics Uspekhi 23, 199 (1980).
- [4] R. von Baltz and W. Kraut, Theory of the bulk photovoltaic effect in pure crystals, Phys. Rev. B 23, 5590 (1981).
- [5] V. Fridkin, Bulk photovoltaic effect in noncentrosymmetric crystals, Crystallography Reports 46, 654 (2001).
- [6] S. Manzeli, D. Ovchinnikov, D. Pasquier, O. V. Yazyev, and A. Kis, 2d transition metal dichalcogenides, Nature Reviews Materials 2, 1 (2017).
- [7] Y. Mao, J. Zhou, M. Grüning, and C. Attaccalite, Shift current in 2d janus transition-metal dichalcogenides: the role of excitons (2025), arXiv:2506.16067 [cond-mat.meshall].
- [8] G. B. Osterhoudt, L. K. Diebel, M. J. Gray, X. Yang, J. Stanco, X. Huang, B. Shen, N. Ni, P. J. W. Moll, Y. Ran, and K. S. Burch, Colossal mid-infrared bulk photovoltaic effect in a type-i weyl semimetal, Nature Materials 18, 471 (2019).

- [9] Z. He and H. Weng, Giant nonlinear hall effect in twisted bilayer wte2, npj Quantum Materials 6, 101 (2021).
- [10] M. Huang, Z. Wu, J. Hu, X. Cai, E. Li, L. An, X. Feng, Z. Ye, N. Lin, K. T. Law, and N. Wang, Giant nonlinear Hall effect in twisted bilayer WSe2, National Science Review 10, nwac232 (2022).
- [11] Y. Mao, C. Attaccalite, and D. G. Ovalle, Moiré amplification of highly tunable shift current response in twisted trilayer graphene, Phys. Rev. B 111, 195408 (2025).
- [12] P. A. Pantaleón, T. Low, and F. Guinea, Tunable large berry dipole in strained twisted bilayer graphene, Phys. Rev. B 103, 205403 (2021).
- [13] J. Duan, Y. Jian, Y. Gao, H. Peng, J. Zhong, Q. Feng, J. Mao, and Y. Yao, Giant second-order nonlinear hall effect in twisted bilayer graphene, Phys. Rev. Lett. 129, 186801 (2022).
- [14] S. Sinha, P. C. Adak, A. Chakraborty, K. Das, K. Debnath, L. D. V. Sangani, K. Watanabe, T. Taniguchi, U. V. Waghmare, A. Agarwal, and M. M. Deshmukh, Berry curvature dipole senses topological transition in a moiré superlattice, Nature Physics 18, 765 (2022).
- [15] C.-P. Zhang, J. Xiao, B. T. Zhou, J.-X. Hu, Y.-M. Xie, B. Yan, and K. T. Law, Giant nonlinear hall effect in strained twisted bilayer graphene, Phys. Rev. B 106, L041111 (2022).

- [16] M. Huang, Z. Wu, X. Zhang, X. Feng, Z. Zhou, S. Wang, Y. Chen, C. Cheng, K. Sun, Z. Y. Meng, and N. Wang, Intrinsic nonlinear hall effect and gate-switchable berry curvature sliding in twisted bilayer graphene, Phys. Rev. Lett. 131, 066301 (2023).
- [17] T. V. Joya, T. Kawakami, and M. Koshino, Shift current response in twisted double bilayer graphene, Phys. Rev. B 112, 085407 (2025).
- [18] D. Kaplan, T. Holder, and B. Yan, Twisted photovoltaics at terahertz frequencies from momentum shift current, Phys. Rev. Res. 4, 013209 (2022).
- [19] J.-X. Hu, Y.-M. Xie, and K. T. Law, Berry curvature, spin hall effect, and nonlinear optical response in moiré transition metal dichalcogenide heterobilayers, Phys. Rev. B 107, 075424 (2023).
- [20] D. Călugăru, F. Xie, Z.-D. Song, B. Lian, N. Regnault, and B. A. Bernevig, Twisted symmetric trilayer graphene: Single-particle and many-body hamiltonians and hidden nonlocal symmetries of trilayer moiré systems with and without displacement field, Phys. Rev. B 103, 195411 (2021).
- [21] S. Chen, S. Chaudhary, G. Refael, and C. Lewandowski, Enhancing shift current response via virtual multiband transitions, Communications Physics 7, 250 (2024).
- [22] Z. Zheng, K. Chang, and J. L. Cheng, Gate voltage induced injection and shift currents in aa- and ab-stacked bilayer graphene, Phys. Rev. B 108, 235401 (2023).
- [23] A. Postlewaite, A. Raj, S. Chaudhary, and G. A. Fiete, Quantum geometry and nonlinear optical responses in rhombohedral trilayer graphene (2024).
- [24] Y. Gao, W. Zou, and C. Zhang, The bulk photovoltaic effect in the one-dimensional interface of graphene/bn superlattice, Physical Chemistry Chemical Physics 10.1039/D5CP03159A (2025).
- [25] S. M. Young and A. M. Rappe, First principles calculation of the shift current photovoltaic effect in ferroelectrics, Phys. Rev. Lett. 109, 116601 (2012).
- [26] L. Z. Tan and A. M. Rappe, Enhancement of the bulk photovoltaic effect in topological insulators, Phys. Rev. Lett. 116, 237402 (2016).
- [27] Y. Zhang, H. Ishizuka, J. van den Brink, C. Felser, B. Yan, and N. Nagaosa, Photogalvanic effect in weyl semimetals from first principles, Phys. Rev. B 97, 241118 (2018).
- [28] Y. Zhang, F. de Juan, A. G. Grushin, C. Felser, and Y. Sun, Strong bulk photovoltaic effect in chiral crystals in the visible spectrum, Phys. Rev. B 100, 245206 (2019).
- [29] Q. Xu, Y. Zhang, K. Koepernik, W. Shi, J. van den Brink, C. Felser, and Y. Sun, Comprehensive scan for nonmagnetic weyl semimetals with nonlinear optical response, npj Computational Materials 6, 32 (2020).

- [30] P. He, H. Isobe, D. Zhu, C.-H. Hsu, L. Fu, and H. Yang, Quantum frequency doubling in the topological insulator bi2se3, Nature Communications 12, 698 (2021).
- [31] R. P. Tiwari, Enhanced shift current bulk photovoltaic effect in ferroelectric rashba semiconductor α -gete: ab initio study from three- to two-dimensional van der waals layered structures, Journal of Physics: Condensed Matter **34**, 435404 (2022).
- [32] P. Feng, Z. Gong, B. Wang, Z. Wang, H. Xu, L. Zou, C. Liu, X. Han, Y. Cheng, B. Yu, et al., High-efficiency bulk photovoltaic effect with ferroelectric-increased shift current, Nature Communications 16, 9839 (2025).
- [33] X. Yang, K. Burch, and Y. Ran, Divergent bulk photovoltaic effect in weyl semimetals (2018), arXiv:1712.09363 [cond-mat.mes-hall].
- [34] V. I. Belinicher and B. I. Sturman, The relation between shift and ballistic currents in the theory of photogalvanic effect, Ferroelectrics 83, 29 (1988).
- [35] J. E. Sipe and A. I. Shkrebtii, Second-order optical response in semiconductors, Phys. Rev. B **61**, 5337 (2000).
- [36] D. E. Parker, T. Morimoto, J. Orenstein, and J. E. Moore, Diagrammatic approach to nonlinear optical response with application to weyl semimetals, Phys. Rev. B 99, 045121 (2019).
- [37] L. Z. Tan, F. Zheng, S. M. Young, F. Wang, S. Liu, and A. M. Rappe, Shift current bulk photovoltaic effect in polar materials—hybrid and oxide perovskites and beyond, npj computational materials 2, 1 (2016).
- [38] Y. Zhang, T. Holder, H. Ishizuka, F. de Juan, N. Nagaosa, C. Felser, and B. Yan, Switchable magnetic bulk photovoltaic effect in the two-dimensional magnet cri3, Nature Communications 10, 3783 (2019).
- [39] Z. Dai and A. M. Rappe, Magnetic bulk photovoltaic effect: Strong and weak field, Phys. Rev. B 107, L201201 (2023).
- [40] L. Gao, Z. Addison, E. J. Mele, and A. M. Rappe, Intrinsic fermi-surface contribution to the bulk photovoltaic effect, Phys. Rev. Res. 3, L042032 (2021).
- [41] J. Ma, Q. Gu, Y. Liu, J. Lai, P. Yu, X. Zhuo, Z. Liu, J.-H. Chen, J. Feng, and D. Sun, Nonlinear photoresponse of type-ii weyl semimetals, Nature materials 18, 476 (2019).
- [42] F. Hipolito, T. G. Pedersen, and V. M. Pereira, Nonlinear photocurrents in two-dimensional systems based on graphene and boron nitride, Phys. Rev. B 94, 045434 (2016).
- [43] A. M. Cook, B. M. Fregoso, F. De Juan, S. Coh, and J. E. Moore, Design principles for shift current photovoltaics, Nature communications 8, 14176 (2017).
- [44] X. Mu, Q. Xue, Y. Sun, and J. Zhou, Magnetic proximity enabled bulk photovoltaic effects in van der waals heterostructures, Physical Review Research 5, 013001 (2023).